

## Flood depth mapping in street photos with image processing and deep neural networks



Bahareh Alizadeh Kharazi<sup>a</sup>, Amir H. Behzadan<sup>b,\*</sup>

<sup>a</sup> Department of Landscape Architecture and Urban Planning, Texas A&M University, 3137 TAMU, College Station, TX 77843, USA

<sup>b</sup> Department of Construction Science, Texas A&M University, 3137 TAMU, College Station, TX 77843, USA

### ARTICLE INFO

**Keywords:**

Water depth  
Flood  
Disaster management  
Image processing  
Deep learning  
Edge detection

### ABSTRACT

Many parts of the world experience severe episodes of flooding every year. In addition to the high cost of mitigation and damage to property, floods make roads impassable and hamper community evacuation, movement of goods and services, and rescue missions. Knowing the depth of floodwater is critical to the success of response and recovery operations that follow. However, flood mapping especially in urban areas using traditional methods such as remote sensing and digital elevation models (DEMs) yields large errors due to reshaped surface topography and microtopographic variations combined with vegetation bias. This paper presents a deep neural network approach to detect submerged stop signs in photos taken from flooded roads and intersections, coupled with Canny edge detection and probabilistic Hough transform to calculate pole length and estimate floodwater depth. Additionally, a tilt correction technique is implemented to address the problem of sideways tilt in visual analysis of submerged stop signs. An in-house dataset, named BluPix 2020.1 consisting of paired web-mined photos of submerged stop signs across 10 FEMA regions (for U.S. locations) and Canada is used to evaluate the models. Overall, pole length is estimated with an RMSE of 17.43 and 8.61 in. in pre- and post-flood photos, respectively, leading to a mean absolute error of 12.63 in. in floodwater depth estimation. Findings of this research are sought to equip jurisdictions, local governments, and citizens in flood-prone regions with a simple, reliable, and scalable solution that can provide (near-) real time estimation of floodwater depth in their surroundings.

### 1. Introduction

Flooding is the most frequent weather threat and costliest natural hazard in the world (Mizutori & Guha-Sapir, 2018). The U.S. National Flood Insurance Program (NFIP) estimates the cost of floods to be over \$1 trillion since 1980 (Smith, 2020). Over the past two decades, there have been close to 5000 flood events in the U.S. alone, leading to approximately 2000 deaths (American Climate, 2019). Flooding can happen as a result of excess rainfall, tropical depressions or storms, hurricanes, or typhoons (Texas General Land Office, 2019). Between 1851 and 2019, for example, the continental U.S. has experienced around 310 hurricane landfalls, averaging to almost 2 hurricanes per year (Texas General Land Office, 2019), including major hurricanes such as Harvey in 2017 which brought unprecedented rainfall and windstorms, and flooded more than 150,000 homes, 46% of which were outside the 500-year floodplain zones of the Federal Emergency Management Agency (FEMA) (Galloway et al., 2018). According to a recent

study, by the year 2100, the amount of land in the U.S. that is vulnerable to a 100-year flood event may increase by 45% in riverine floodplains, and 55% in coastal floodplains with fixed shorelines (e.g., stabilized through beach nourishment and other activities; AECOM, 2013). As sea levels rise (Church & White, 2011), many communities, especially those in coastal areas, will experience growing risks and differential vulnerability to floods and storm water surge (Alfieri et al., 2017; Cletus, 2013; Ford et al., 2019; Garner et al., 2018; Hauer, Evans, & Mishra, 2016). In the U.S. State of Texas, for instance, the State Hazard Mitigation Plan (SHMP) estimates \$6.87 billion in property losses and around 2000 injuries and fatalities caused by a combination of coastal and riverine floods between 2018 and 2023 (Texas General Land Office, 2019). In Europe, strong mitigation incentives are expected to lead to a double increase in the average risk-based flood insurance premium between 2015 and 2050 (Hudson, Botzen, & Aerts, 2019).

In the aftermath of large-scale natural hazard events such as floods and hurricanes, having access to timely and accurate information is key

\* Corresponding author.

E-mail addresses: [bahareh.alizadeh@tamu.edu](mailto:bahareh.alizadeh@tamu.edu) (B. Alizadeh Kharazi), [abehzadan@tamu.edu](mailto:abehzadan@tamu.edu) (A.H. Behzadan).

not only to successful response and recovery (Gebrehiwot, Hashemi-Beni, Thompson, Kordjamshidi, & Langan, 2019; Pi, Nath, & Behzadan, 2020), but also to mitigation, which aims to protect the health and safety of people, and limit damage to property or the environment (Federal Emergency Management Agency, 2016; Public Safety Canada, 2010). First responders and emergency managers deployed from different jurisdictions (e.g., local governments, humanitarian agencies, non-government organizations) to a disaster-affected area follow their own command structure, abide by different standard operational procedures, and more importantly, use various communication and data exchange platforms which may not be compatible with one another or accessible to all participating teams (FEMA, 2016; Texas General Land Office, 2019). Moreover, much of the information from the field remains unseen by ordinary people who are the most affected, leading them to seek help through other channels, thus quickly overwhelming the telecommunication network. For instance, during Hurricane Harvey, trapped people dialed non-emergency numbers such as 2-1-1 or 3-1-1 which only connected them to community services and information, or municipal government services (Texas General Land Office, 2019). A decentralized yet authenticated platform for collecting immediate multi-faceted data about the unfolding hazard event, and sharing timely and accurate information with all stakeholders could potentially remedy this problem.

In particular to flood events, knowing the depth of water and the location of flood inundated areas and submerged lands are key descriptors of the risk to human life and the extent of property damage. Flooded roads hamper community evacuation, movement of goods and services, and ground rescue missions. In Texas alone, an estimated 75% of flood-related deaths occur when people travel on local roads to evacuate without knowing the depth of flood in their surroundings (Texas General Land Office, 2019). With respect to flood-induced property damage, only 1 in. of floodwater can cause \$27,000 in combined damages to an average one-story home (FloodZone, 2018), and 1–2 ft of water floats and sweeps away many vehicles. While floodwater permeates natural surfaces such as gravel, turf, and non-compacted soil, impervious surfaces in urban areas made with asphalt or concrete can cause excess water run-off on roads (Collins, Hunt, & Hathaway, 2007). What further complicates this problem is that floodwater moves and water level changes over time, which necessitates (near-) real time calculation of floodwater depth so that communities and first responders can avoid flooded areas and passages during evacuation and search and rescue (SAR) operations. In Hurricane Katrina, for example, emergency responders were frequently requesting information about the extent of flood and floodwater depth to deploy the right type of vehicles for SAR missions and determine the best route for accessing victims (Nayak & Zlatanova, 2008). In the absence of such data, people tend to rely on various social media posts or news stories on learn about the level of flooding and destruction in their neighborhoods (Fan et al., 2020; Nayak & Zlatanova, 2008). Excessive exposure to post-disaster media coverage, however, has been shown to contribute to stress, anxiety, and long-term psychological outcomes (Ten Veen, Morren, & Yzermans, 2009).

## 2. Literature review

Historically, the most common tool to inform communities about the local flood risk has been FEMA flood maps (Federal Emergency Management Agency, 2010). Flood maps set minimum floodplain standards and serve as the basis for determining the cost of flood insurance, which provides property owners with some level of financial protection (Federal Emergency Management Agency, 2010). However, approximately 75% of FEMA flood maps are older than 5 years, and 11% date back to the 1970s and 80s (First Street Foundation, 2019). A 2017 report by the U.S. Department of Homeland Security's Office of Inspector General found that only 42% of the total flood map miles in FEMA's inventory were updated and valid, falling short of FEMA's internal performance goal of 80% (Department of Homeland Security Office of Inspector

General, 2017). At present, many parts of the U.S. do not have flood maps or have maps that are 15–30 years old (First Street Foundation, 2019).

Conventional methods of flood depth calculation utilize data from water depth sensors or water wells in predefined locations. The U.S. Geological Survey (USGS), for example, operates a little more than 9500 flood gages nationwide that transmit rainfall amounts and/or stream levels (National Oceanic and Atmospheric Administration, 2020). Researchers have also used hydrostatic pressure, mechanical float systems, thermal conductivity, and radiation-based water level measurement methods (Chetpattananondh, Tapoano, Phukpattaranont, & Jindapetch, 2014). Previous work has attempted to predict flooding by detecting the rise or fall of water levels by comparing sensor readings with predefined thresholds (Chetpattananondh et al., 2014; Odli et al., 2016; Töyrä, Pietroniro, Martz, & Prowse, 2002). These sensors, however, have limited coverage area (primarily in and around riverine or coastal lands), can be washed away in heavy rain, and need major effort for installation, calibration, and maintenance in flood susceptible locations.

Researchers have also used computer models to estimate flood depth and flow characteristics. However, surface variability and inconsistency coupled with the difficulty in differentiating saturated surface soil and standing water in aerial images makes it difficult for these models to achieve accurate results especially in urban areas (Salmonsson, 2015; United States Geological Survey, 2019). Additionally, most existing global digital elevation models (DEMs) used for flood mapping are dated and insensitive to reshaped surface topography, and acquisitions are not routinely repeated (Hawker, Bates, Neal, & Rougier, 2018). DEMs tend to result in large vertical errors especially over complex topography (e.g., urban areas), exhibit little microtopographic variations in relatively flat terrain, and suffer from vegetation bias (Baugh, Bates, Schumann, & Trigg, 2013; O'Loughlin, Paiva, Durand, Alsdorf, & Bates, 2016), rendering them unreliable for resolving key terrain features that control flood characteristics (Schumann, 2014). In a study that assessed several large-scale DEMs for hydrologic runoff prediction, it was concluded that different DEMs can lead to almost 10% in runoff prediction error (Kenward, Lettenmaier, Wood, & Fielding, 2000). In developing Floodwater Depth Estimation Tool (FwDET), based solely on an inundation map with an associated DEM, researchers reported an average difference of 18 cm and 31 cm for selected coastal (using a 1-m DEM) and riverine (using a 10-m DEM) areas compared to physically-based hydrodynamic simulations (Cohen, Raney, Munasinghe, & Loftis, 2019). In some cases, even high-accuracy DEMs from aerial photogrammetry may be significantly different from ground truth, especially when looking at smaller catchments or applications for which localized elevation errors can be detrimental to local scale applications (Walker & Willgoose, 1999).

More recently, advancements in machine learning (ML) for object detection have led to new opportunities for remotely estimating water level using computer vision algorithms. Yang, Wang, and Yang (2014), for instance, used visual recognition to read water levels from a video camera set up alongside a river embankment in order to predict flood due to rising water levels. They utilized Laplacian method (Vincent & Folorunso, 2009) for detecting the edges of different objects and probabilistic Hough transform (Zhu & Brilakis, 2009) for detecting the straight waterline. Testing this method on an indoor water channel and in simulated rainfall resulted in less than 1.2% and 2.5% in average absolute error, respectively. Dong, Yu, Farahmand, and Mostafavi (2020) simulated the failure cascade process and flood control network vulnerability with a Bayesian method based on the topological structure of the flood control network. Pan et al. (2018) calculated water level by remotely monitoring the length of a measuring ruler (in pixels) in footage obtained from a video camera installed next to a river, and found that convolutional neural networks (CNNs) outperformed traditional image processing algorithms with an average error of 9 mm and a standard deviation of 6.69 mm. Park, Baek, Sohn, and Kim (2021)

estimated the depth of flood through detecting submerged vehicles in flood photos using Mask R-CNN (He, Gkioxari, Dollár, & Girshick, 2017), and comparing them with the most similar 3D rendered objects based on feature maps extracted by VGGNets (Simonyan & Zisserman, 2015). Using features extracted from the 4th pooling layer of VGG16, they achieved mean absolute error values as low as 6.49 cm. Other than cameras, drone and satellite imagery have been used for detecting floods using visual information. For example, in a study by Gebrehiwot et al. (2019), flooded areas were found from videos captured by a drone using four object detection methods based on different variations of fully convolutional networks (FCN-16, FCN-18, FCN-32) (Long et al., 2015) and support vector machines (SVM) (Cortes & Vapnik, 1995) with an accuracy of 95%, 95.52%, 92% and 87.45%, respectively. Pi et al. (2020) trained a CNN model on VOC dataset (Everingham, Van Gool, Williams, Winn, & Zisserman, 2010) to detect flooded areas with a mean average precision (mAP) of 80.69% in aerial videos.

Besides the high cost of sensor installation and operation for real time data acquisition, a key challenge in floodwater depth analysis especially in urban settings is the lack of granularity of flood information in comparison with roads and neighborhood data, which makes it extremely difficult to contextualize the relationship between the road network and flooded areas. Recently, light detection and ranging (LiDAR) (Kwan & Ransberger, 2010; McDougall & Temple-Watts, 2012), structure from motion (SfM) (Meesuk, Vojinovic, & Mynett, 2017), and the U.S. Geological Survey (USGS) National Water Information System (United States Geological Survey, 2019) have been used to map flood events and determine the flow path to estimate floodwater depth, albeit their application is limited to places that are fully visible from air and not obscured by vegetation or bridges (United States Geological Survey, 2019). At present, precise measurement of water depth (i.e., with centimeter-level accuracy) from aerial views is mostly done with highly sophisticated instruments and expensive computations that are not readily available for large-scale adoption (United States Geological Survey, 2019).

The core contribution of this study is a novel and easy-to-use benchmarking method (using traffic signs) for calculating the floodwater depth at street-level. While CNNs have been previously used to detect everyday objects (including traffic signs), this study expands the application of these models by incorporating edge and line detection methods for calculating the length of the sign pole through image processing and tilt correction techniques. The outcome of this work equips jurisdictions, local governments, and citizens in flood-prone regions with a simple, reliable, and scalable solution that can provide (near-) real time and accurate estimation of floodwater depth in their surroundings.

### 3. Methodology

In this research, a low-cost image processing technique (comprised of CNNs, and edge and line detection models) is utilized to measure floodwater depth. The model input is a pair of pre- and post-flood street photos taken by ordinary handheld devices (e.g., smartphones, tablet computers, digital cameras), and the output is the depth of floodwater at the location where the photos were taken. While images can be taken from different angles and different distances from the water surface, to measure the depth of the flood, the model relies on the dimensions of a known benchmark visible in the image, for which the real size (e.g., in inches) is known. Image processing is then used to determine the size of this benchmark in pixels and calculate a constant measurement ratio (e.g., inches to pixel), which in turn, is used to convert all other measurements from pixel to standard units (e.g., inches).

Past research has investigated the use of various objects for flood depth estimation. For instance, Barz et al. (2019) proposed an image retrieval approach with relevance feedback to find flood images on social media. Sazara, Cetin, and Iftekharuddin (2019) trained deep neural networks to recognize flooded roads in photos taken by mobile devices.

In another research, the size of submerged objects in water was used to estimate the depth of flood with a mean absolute error of approximately 10 cm (Chaudhary, D'Aronco, Moy de Vitry, Leitão, & Wegner, 2019). In contrast to past work that has used objects with arbitrary shapes and sizes as benchmarks, to increase practicality in real world flood response operations, the visual benchmark selected in this research is ubiquitous (i.e., existing in many places), and has standardized shape and dimensions that are known to the model beforehand. In addition, to maximize scalability and increase technology adoption among users, the benchmark should be relatable, and easy to find and access. This last requirement is of particular importance when crowdsourcing is the main source of flood data collection, as past research has indicated that participants should be continuously kept motivated and engaged to complete delegated tasks with expected quality (Puttinaovarat & Horkaew, 2020; Sazara et al., 2019). Considering these factors, traffic signs are used in this paper as standard visual benchmarks. Unlike sophisticated flood measurement sensors, traffic signs are omnipresent and easy to identify. In a study by Shinar, Dewar, Summala, and Zakowska (2003), 78% of local traffic signs were perfectly identified by people (regardless of age or group). Stop signs, in particular, can be found in many intersections in urban and rural areas. Boeing (2018) used OpenStreetMap to analyze 27,000 U.S. street networks and counted approximately 50 intersections per 1 km<sup>2</sup> of neighborhood-scale street network. While the exact number of stop signs in the U.S. is a matter of debate, it is a fact that many intersections feature two-way or four-way stop signs to control traffic flow especially when there is high-speed traffic, restricted view, or pedestrian crossing (Federal Highway Administration, 2009). In many parts of the world, a stop sign is easily recognizable by its octagonal shape with standardized equal height and width. In the U.S., traffic sign shapes and dimensions are laid out in the Manual on Uniform Traffic Control Devices (MUTCD) and its companion volume, Standard Highway Signs (SHS) (Federal Highway Administration, 2004). The size of a stop sign may slightly vary depending on the location it is installed; 30 × 30 in. in single-lane roads (almost all residential neighborhoods), and 36 × 36 in. in multi-lane conventional roads and expressways. While the shape and dimensions of the sign itself is standardized, the pole that holds it may or may not be regulated and can be made of different material and have different length.

As shown in Fig. 1, the depth of floodwater, i.e.,  $d_w$ , can be calculated as the difference between pole lengths in paired pre- and post-flood photos. In Fig. 1(a), knowing the height of the sign octagon in both pixels ( $s$ ) and in inches (30"), the constant ratio  $r$  is obtained as  $30/s$ , indicating the number of inches corresponding to one pixel in the post-flood photo. Using this ratio, the length of the pole above waterline is calculated as  $r \times p$ , in which  $p$  is the pole length in pixels. Similarly, In Fig. 1(b), knowing the height of the sign octagon in pixels ( $s'$ ) and inches (30", same as before), the constant ratio  $r'$  is obtained as  $30/s'$ , indicating the number of inches corresponding to one pixel in the pre-flood photo. Using this ratio, the full length of the pole (with no floodwater) is calculated as  $r' \times p'$ , in which  $p'$  is the pole length in pixels. Note that ratios  $r$  and  $r'$  are not necessarily equal since the two photos could be taken at different angles and distances from the stop sign. The following Subsections describe how pixel dimensions  $s$ ,  $p$ ,  $s'$ , and  $p'$  are extracted with image processing.

#### 3.1. Stop sign detection

In order to detect and generate a mask (pixel boundaries) of the stop sign in the input image, a modified version of Mask R-CNN (He et al., 2017), which uses RetinaNet (Lin, Goyal, Girshick, He, & Dollár, 2017) for regression, classification, and mask estimation, is implemented based on Keras open-source library (Gulli & Pal, 2017). Mask R-CNN is a deep neural network that is pre-trained on the COCO image dataset (containing 80 classes) for instance segmentation (Lin et al., 2014). In this research, any classes other than stop signs are filtered out during

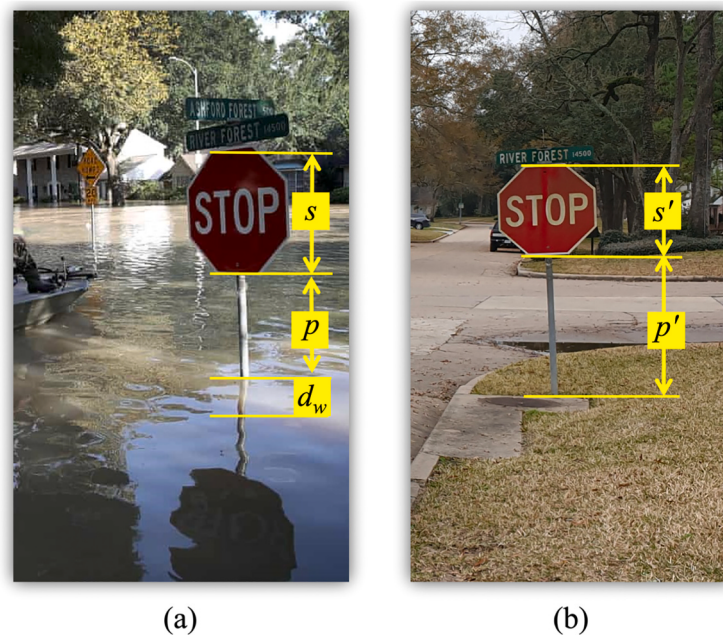


**Fig. 1.** A stop sign in a residential neighborhood (Houston, Texas), paired in (a) post-flood photo, and (b) pre-flood photo. (base post-flood photo: courtesy of Win McNamee/Getty Images).

mask detection. As shown in Fig. 2, the Mask R-CNN architecture internally combines two smaller networks, Faster R-CNN (Ren, He, Girshick, & Sun, 2015) for detecting objects, and an FCN (Lin et al., 2017) for understanding the image context. The loss function of Mask R-CNN is therefore the sum of the loss functions of these two networks.

Faster R-CNN utilizes region proposal network (RPN) (Ren et al., 2015) to generate region proposals, followed by a secondary network that uses these proposals to detect objects and draw bounding boxes. The output of the RPN consists of proposed regions with different sizes, leading to differently sized feature maps. Prior to classification and bounding box regression, these feature maps should be reduced to the same size. To this end, region of interest (ROI) pooling (Girshick, 2015) is used to split the input feature map into a fixed number of roughly equal regions, followed by max pooling on every region. The final output

of the Faster R-CNN is class labels (classification) and bounding boxes (localization). To generate object masks inside each bounding box, FCN decompresses the image to 1/32 of its original size with blocks of convolution and max pooling layers to capture contextual and semantic information. Next, class prediction is made, and the image is rescaled to its original size with deconvolution layers and upsampling to return spatial information that were lost during downsampling. To minimize information loss, spatial data is transferred before downsampling with a skip connection (Long et al., 2015). Fig. 2 shows the overall architecture of the Mask-RCNN consisting of two internal networks and the flow of image processing through each part.

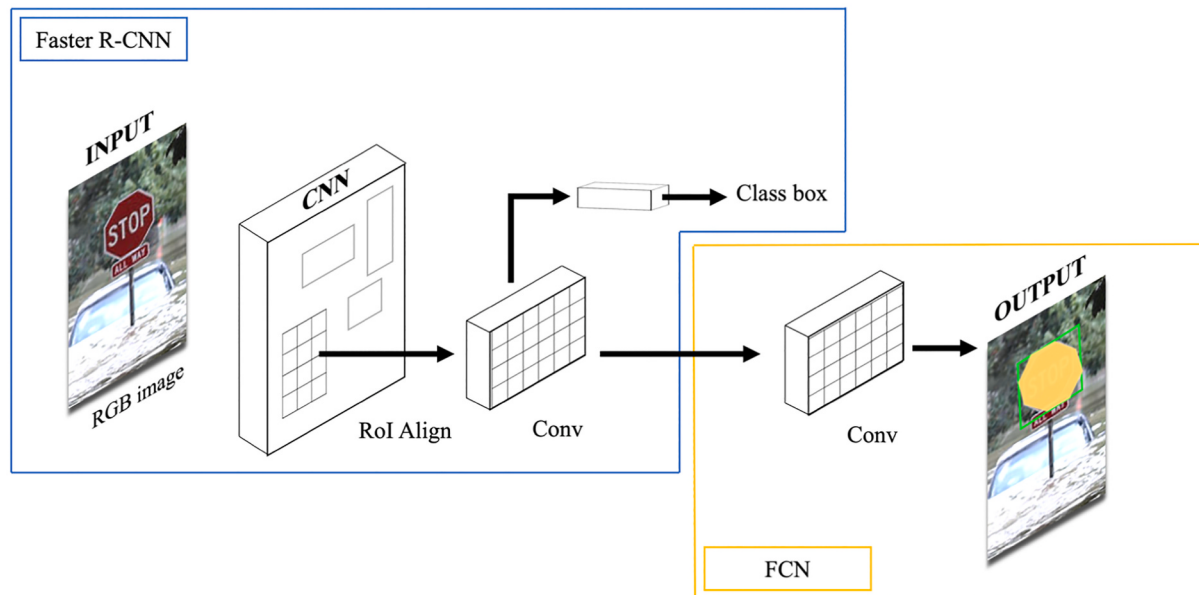


**Fig. 2.** Overall architecture of the Mask R-CNN implementation. (base flood photo: courtesy of Win McNamee/Getty Images).

### 3.2. Pole detection

Pole detection is performed in a two-step process using pre- or post-flood photos with generated stop sign masks from [Section 3.1](#). First, all edges in the grayscale input image are discovered using Canny edge detector ([Rong, Li, Zhang, & Sun, 2014](#)), and next, probabilistic Hough transform for straight line detection is utilized to create a list of pole candidates by selecting edges that form lines. To implement Canny edge detector ([Wang, 2013](#)), images are first converted from the original red-green-blue (RGB) color space to grayscale using Eq. (1), in which  $pix_c$ ,  $pix_r$ ,  $pix_g$ , and  $pix_b$  represent the grayscale, red, green, and blue values of each pixel, respectively.

$$pix_c = 0.3 \times pix_r + 0.59 \times pix_g + 0.11 \times pix_b \quad \text{Eq. (1)}$$

The raw output of the Canny edge detector is an edge map which consists of all detected edges (regardless of angle and position) in the image. To reduce noise in the image, a  $5 \times 5$  Gaussian filter replaces the value of each pixel with the weighted average of its adjacent pixels. This eliminates false positives and edges that are the least consequential (e.g., lines that appear too small, or are too far away). As shown in Eq. (2), the  $5 \times 5$  Gaussian filter is applied (through a convolution operation,  $*$ ) to the input image  $Img_i$  to generate an output image  $Img_o$  with smoothed noise. Evidently, the size of the Gaussian filter can affect the outcome of edge detection. Generally, while a larger filter size lowers the sensitivity to noise, it may as well increase the localization error ([Pedersini, Sarti, & Tubaro, 1997](#)). However, previous work has shown that a  $5 \times 5$  filter is suitable in most cases ([Delgado, 2018](#); [Hsiao, Chen, Chou, Li, & Chen, 2006](#)).

$$Img_o = \frac{1}{159} \begin{bmatrix} 2 & 4 & 5 & 4 & 2 \\ 4 & 9 & 12 & 9 & 4 \\ 5 & 12 & 15 & 12 & 5 \\ 4 & 9 & 12 & 9 & 4 \\ 2 & 4 & 5 & 4 & 2 \end{bmatrix} * Img_i \quad \text{Eq. (2)}$$

Next, the intensity gradient of each detected edge in  $Img_o$  is determined by a Sobel filter ([Sobel, 1978](#)) which returns a value for the first derivative in the horizontal direction ( $G_x$ ) and vertical direction ( $G_y$ ). Using these two values, the edge gradient ( $G$ ) and direction ( $\theta$ ) are determined using Eqs. (3) and (4). The calculated gradient is always perpendicular to the edge.

$$G = \sqrt{G_x^2 + G_y^2} \quad \text{Eq. (3)}$$

$$\theta = \tanh^{-1}(G_x/G_y) \quad \text{Eq. (4)}$$

Following the gradient calculation, an edge thinning technique called non-maximum suppression is used to compare the edge strength of each pixel with that of the pixel in the positive and negative gradient directions, and subsequently remove pixels that are not local maximums in the direction of the edge gradient ([Rong et al., 2014](#)). The output of this stage is a binary (i.e., grayscale) image of remaining edge pixels providing a more accurate representation of real edges in the image. This image is processed with hysteresis thresholding, a noise reduction step to determine if weak edge pixels (e.g., pixels detected as edges because of noise or color variation) should be kept or eliminated from the final image. The literature on Canny edge detector has proposed different values for minimum and maximum thresholds based on image type and application. Some have used fixed values of 100 and 300 for lower and upper thresholds, respectively ([OpenCV Dev Team, 2019](#); [Wang, 2013](#)). Alternatively, threshold values can be determined based on the pixel values of an image ([Farras, 2020](#); [Liang, n. d.](#)). More advanced methods involve automated Canny edge thresholding using a Gaussian Kernel, and fuzzy logic-based threshold selection ([Incetas, Demirci, & Yavuzcan, 2019](#); [Powers, 2011](#); [Tanyeri, Kiliçsan, & Demirci, 2019](#)). Considering the content and diversity of flood photos used in this study, upper and lower thresholds for edge detection are

constructed based on percentages of the median of pixel intensities in the image. Minimum and maximum threshold values serve as the basis to determine whether a pixel belongs to an edge (if its intensity gradient is more than the upper threshold) or must be discarded (if its intensity gradient is less than the lower threshold). A pixel with an intensity gradient between the lower and upper thresholds is assessed in the context of its neighboring connections; if it is connected to a strong edge pixel, it will be kept as part of that edge, and otherwise it will be marked as a non-edge pixel. [Fig. 3](#) shows the steps of the Canny edge detection process applied to a sample flooded stop sign image.

Next, probabilistic Hough transform is utilized to detect straight lines in the output image of Canny edge detector as potential pole candidates. Probabilistic Hough transform is commonly used to isolate features of a parametrically defined shape (e.g., line, circle, ellipse) within an image by a voting procedure ([Li, Yin, Zhi, & Duan, 2020](#)). Using this technique, the image coordinate system is transformed from the Cartesian space ( $x, y$ ) to a polar space ( $\rho, \theta$ ) using Eq. (5) in which,  $\rho > 0$  and  $0 \leq \theta \leq 2\pi$ .

$$\rho = x \cos \theta + y \sin \theta \quad \text{Eq. (5)}$$

The premise of probabilistic Hough transform is that if values defined by each edge pixel are plotted, points in the Cartesian space map to curves in the polar Hough parameter space. This point-to-curve transformation denotes the Hough transformation for straight lines. When viewed in Hough parameter space, points that are collinear in the Cartesian space become apparent as they form curves which intersect a common  $(\rho, \theta)$  point. Four thresholds are defined, i.e., minimum line length ( $L_{min}$ ), maximum allowed gap between points on the same line to link them ( $L_{gap}$ ), accumulator threshold parameter that represents the number of votes for each line candidate ( $L_{threshold}$ ), and distance resolution of the accumulator in pixels ( $L_{rho}$ ). In this research, subsets of candidate points are randomly picked, and threshold values are empirically selected as  $L_{min} = 30$ ,  $L_{gap} = 10$ ,  $L_{threshold} = 30$ , and  $L_{rho} = 1$  for pre-flood photos, and  $L_{min} = 30$ ,  $L_{gap} = 10$ ,  $L_{threshold} = 80$ , and  $L_{rho} = 1$  for post-flood photos. The primary reason behind selecting two different  $L_{threshold}$  values for pre- and post-flood photos is the background noise; in pre-flood photos, more line segments are needed to approve the pole line, while in post-flood photos, pole line can be identified with fewer line segments. The output of this step is a vector of matched endpoints of the detected straight and curved lines. For best results, tilt correction ([Section 5.1](#)) is applied to all photos to ensure poles are in near vertical position prior to the application of Hough transform for detecting straight lines. With stop sign poles in near vertical position, only detected lines that are almost vertical are kept. Note that for a given image, the  $x$ -axis runs from left to right, and the  $y$ -axis runs from top to bottom with the origin in the top left corner. Several other problem-specific assumptions are made to reduce noise and confine the solution space to a desired region within the image (i.e., pole is expected to appear under the sign), ultimately leading to an improved output. In particular,

- a. The top of the pole is attached to the midpoint of the bottom edge of the octagon sign. The coordinates of this point,  $(x_{coo}, y_{coo})$ , are calculated from the geometry of the bounding box detected by the Mask R-CNN model ([Section 3.1](#)). In particular,  $x_{coo}$  (measured along the horizontal axis of the image) is calculated by taking the average of the  $x$  coordinates of the lower corners of the bounding box (i.e.,  $x_3$  and  $x_4$ ), while  $y_{coo}$  is equal to the  $y$  coordinate of one of the lower corners of the bounding box ( $y_{coo} = y_3 = y_4$ ). This is shown in [Fig. 4](#).
- b. The bottom of the pole always touches the ground (in pre-flood photos) or the waterline (in post-flood photos). If the pole is not titled, then the  $x$  coordinates of the top and bottom points of the pole are (almost) the same. In this case, the solution space (i.e., where pole is likely to be located) is horizontally confined along the  $x$  axis to  $(x_{coo} - w, x_{coo} + w)$ . The value of  $w$  can be empirically selected without excessively lowering the accuracy of line detection. In this

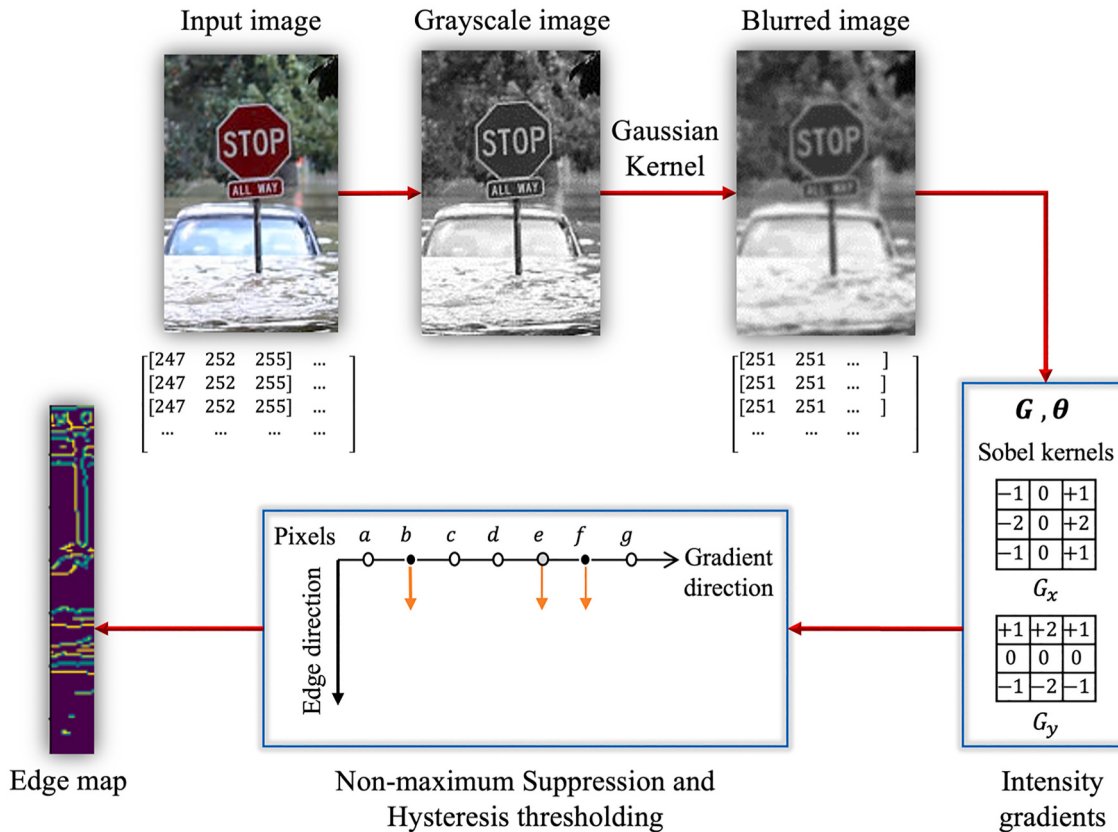


**Fig. 3.** Canny edge detection process applied to a flood image. (base flood photo: courtesy of Win McNamee/Getty Images).

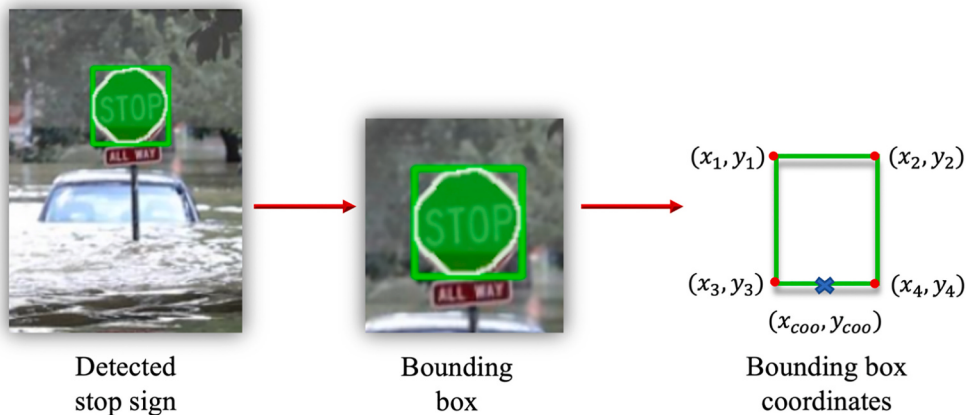


**Fig. 4.** Determining the intersection point of the sign and pole from the stop sign bounding box. (base flood photo: courtesy of Win McNamee/Getty Images).

research,  $w$  is set equal to half of the octagon side ( $S_{oct}$ ), as shown in Fig. 5.

- c. The vertical length of the solution space ( $h$ ) extends from the bottom edge of the octagon sign down to the bottom edge of the image, as shown in Fig. 5.
- d. In some cases, multiple vertical lines are detected under the octagon sign as pole candidates in close proximity from one another (e.g., due to visual inconsistencies such as different shades, colors, or textures). This situation is reconciled by directly connecting  $(x_{coo}, y_{coo})$  to the endpoint that has the maximum  $y$  coordinate value among all detected endpoints, i.e.,  $y = y_{max}$ . The pole length is then calculated by measuring the distance between  $y_{coo}$  and  $y_{max}$ , as shown in Fig. 6.

#### 4. Data description

A large number of flood photos are taken by people, emergency managers, and rescue teams in the aftermath of flood events. Many of these photos, particularly those taken in urban areas, depict various traffic signs including stop signs that are submerged in floodwater. To test the methodology described in Section 3, publicly available flood photos that contain at least one visible stop sign are web-mined using keywords such as “street”, “stop sign”, and “flood” among others. For each photo, available geotag information including location (country, state/province, city, global coordinates), flood event name (if known), dates photo was taken and saved, and source (web link) is also extracted. Next, each post-flood photo is paired with a pre-flood photo of the same location containing the same stop sign, taken from Google Street View

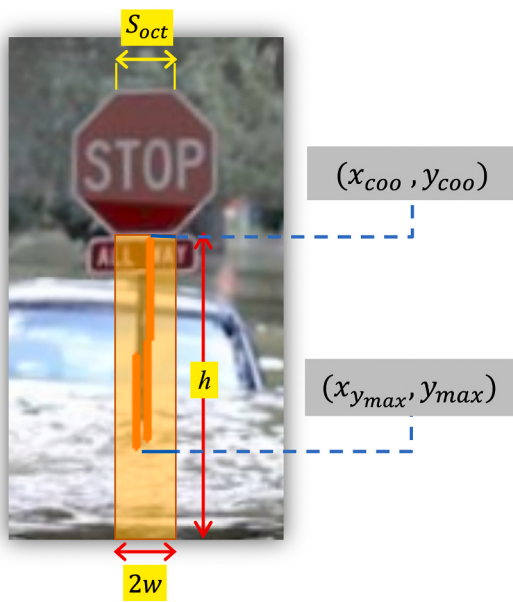


**Fig. 5.** Confining the line detection solution space. (base flood photo: courtesy of Win McNamee/Getty Images).

API. The average time to pair a post-flood photo with the correct pre-flood photo can range from a few minutes (easy pairing, when geotag information is available) to 30 min (difficult pairing through excessive manual search or personal experience, with no geotag information). For each pre-flood photo, longitude and latitude data, as well as a link to the exact location on Google Maps are stored as meta-data.

The dataset, named BluPix 2020.1, contains 186 paired photos of submerged stop signs that are processed by Mask R-CNN ([Section 3.1](#)), and Canny edge detector and probabilistic Hough transform ([Section 3.2](#)). Of these, 173 photos depict U.S. locations, and the remaining 13 photos are from locations in Canada. [Table 1](#) show the geographical distribution of these photos across 10 FEMA regions ([Ogawa, Ito, & Nakano, 2010](#)) and Canada. As shown in this Table, the majority of paired photos (46%) in the U.S. belongs to FEMA region IV which covers locations in Alabama, Florida, Georgia, Kentucky, Mississippi, North Carolina, South Carolina, Tennessee, followed by region VI which contains Arkansas, Louisiana, New Mexico, Oklahoma, and Texas. A temporal analysis of BluPix 2020.1 dataset reveals that 136 paired photos

were taken from flood events that took place between 2011 and 2020, while 12 were taken from flood events that took place between 2000 and 2010, and 1 was taken prior to 2000, with the remaining missing date information. In particular, 93 flood photos were taken since 2017 which coincides with several highly active water-related events including Hurricane Harvey in Texas (FEMA Region VI) during which many people-contributed photos were posted on social media.

Furthermore, 91% of flood photos were published on Google image repository (a.k.a., Google Images), 6% were accessed from Facebook, and other social media sites (i.e., Twitter, Pinterest) accounted for 1% or less of all photos in BluPix 2020.1 dataset. An interesting observation that in part motivated this research is that aside from Google, which is considered a search engine rather than a crowdsourcing platform, there is no dedicated online tool or website for ordinary people to upload flood photos, which adds to the already complex problem of collecting and analyzing these photos for the purpose of calculating and sharing floodwater depth information.

## 5. Results and analysis

To prepare the ground truth information, all stop signs and pole objects in the dataset are separately labeled. [Fig. 7](#) shows ground truth

**Table 1**

Number of paired flood photos in BluPix 2020.1 dataset in each FEMA region and Canada.

Region	Paired photos	Locations included
I	7	Connecticut, Maine, Massachusetts, New Hampshire, Rhode Island, Vermont
II	13	New Jersey, New York, Puerto Rico, U.S. Virgin Islands
III	17	Delaware, Maryland, Pennsylvania, Virginia, West Virginia, District of Columbia
IV	42	Alabama, Florida, Georgia, Kentucky, Mississippi, North Carolina, South Carolina, Tennessee
V	17	Illinois, Indiana, Michigan, Minnesota, Ohio, Wisconsin
VI	38	Arkansas, Louisiana, New Mexico, Oklahoma, Texas
VII	21	Iowa, Kansas, Missouri, Nebraska
VIII	4	Colorado, Montana, North Dakota, South Dakota, Utah, Wyoming
IX	13	Arizona, California, Hawaii, Nevada, American Samoa, Guam, Northern Mariana Islands, Marshall Islands, Micronesia
X	1	Alaska, Idaho, Oregon, Washington
Canada	13	Alberta, British Columbia, Ontario, Quebec, Queensland

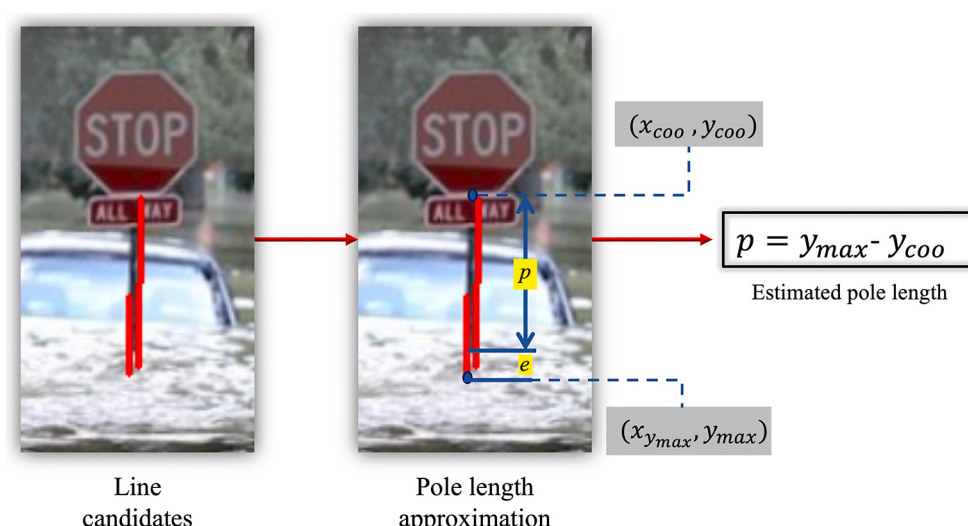


**Fig. 6.** Approximating the stop sign pole from multiple close line candidates. (base flood photo: courtesy of Win McNamee/Getty Images).

examples in pre- and post-flood photos. This information is later used to determine the accuracy of Mask R-CNN ([Section 3.1](#)) in detecting stop sign masks, and Canny edge detector and probabilistic Hough transform ([Section 3.2](#)) in estimating pole lengths. Data processing is conducted on a Lenovo ThinkPad laptop computer with 7 cores, 9750H CPU, 16 GB RAM, and Nvidia Quadro T1000 GPU with a 4 GB memory.

To evaluate the performance of Mask R-CNN, the intersection over union (IoU) of detected and ground-truth masks is calculated by dividing the overlapping area between the two masks by their union area. IoU is a validated accuracy metric in object detection ([He et al., 2017; Huang, Huang, Gong, Huang, & Wang, 2019; Pi et al., 2020](#)). In addition to IoU, precision and recall are determined using Eqs. [\(6\)](#) and [\(7\)](#). In these Equations, true positive (TP) and true negative (TN) refer to the number of correct detections; TP indicates positive detections that are correct, while TN indicates negative detections that are correct. On the other hand, false positive (FP) and false negative (FN) refer to the number of incorrect detections; FP indicates positive detections that are incorrect, while FN indicates negative detections that are incorrect ([Powers, 2011](#)).

$$\text{Precision} = \frac{\text{TP}}{\text{TP} + \text{FP}} \quad \text{Eq. (6)}$$

$$\text{Recall} = \frac{\text{TP}}{\text{TP} + \text{FN}} \quad \text{Eq. (7)}$$

Next, average precision (AP) is calculated by plotting precision as a function of recall and calculating the area under the curve ([Dunham, 2007](#)). From all 186 photos in BluPix 2020.1 dataset, 27 are excluded since they only depict partially visible stop sign or sign pole. In the remaining 159 paired photos, stop signs are successfully detected in 142 pre-flood and 151 post-flood photos, resulting in 89.31% and 94.97% recall, respectively. [Table 2](#) summarizes the performance of stop sign detection task in pre- and post-flood photos.

To evaluate the performance of Canny edge detector and probabilistic Hough transform for straight line detection, estimated pole length is compared with ground truth length, and the root mean square error (RMSE) is calculated using Eq. [\(8\)](#), in which,  $p$  and  $p'$  are detected and ground truth lengths in pixels, respectively ([Fig. 1](#)). Several visual features in analyzed photos lead to misdetection or highly erroneous pole detection. For pre-flood photos, for example, the top three sources of error include image background ( $Er_p = 50.78"$  for 6 photos with cluttered background), pole sideways tilt ( $Er_p = 33.90"$  for 4 photos with

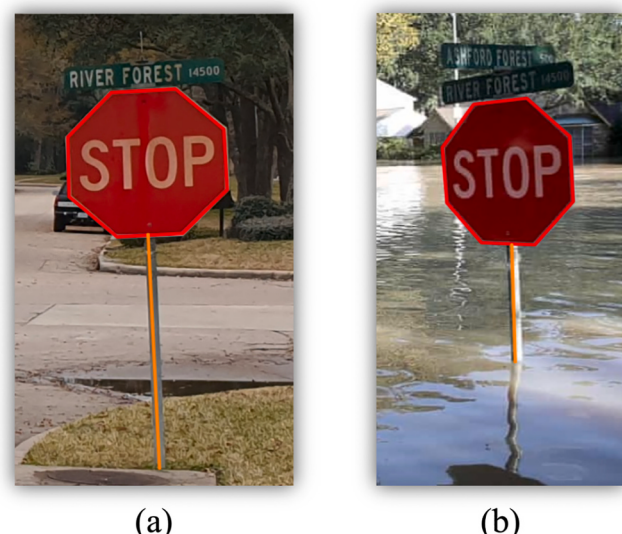


**Fig. 7.** Ground truth annotation in (a) pre-flood photo, and (b) paired post-flood photo. (base post-flood photo: courtesy of Win McNamee/Getty Images).

**Table 2**

Performance of stop sign detection in pre- and post-flood photos.

Metric	Pre-flood	Post-flood
	$n = 159$	$n = 159$
IOU (%)	93.36	92.29
Precision (%)	100	100
Recall (%)	89.31	94.97
AP (%)	89.31	94.97
Processing time (s)	2.23	2.85

excessive pole tilt), and pole shape ( $Er_p = 33.73"$  for 8 photos with unusual pole shape). Similarly, for post-flood photos, the top three sources of error include wavy water surface ( $Er_p = 69.80"$  for 45 photos), water reflection ( $Er_p = 55.53"$  for 47 photos with pole reflection in water), and pole sideways tilt ( $Er_p = 16.93"$  for 5 photos with excessive pole tilt). Detection error due to the pole sideways tilt is further investigated in [Section 5.1](#) since this source of error is a common issue in both categories of pre- and post-flood photos. A discussion of other error types, i.e., water reflection, pole shape, background effects, and image resolution, is beyond the scope of this paper, and will be pursued as part of the future work in this research.

$$Er_p = \sqrt{\frac{1}{N} \sum_{m=1}^N (p - p')^2} \quad \text{Eq. (8)}$$

[Table 3](#) summarizes the performance of pole detection task in a subset of 42 pre-flood and 42 post-flood photos that were ultimately selected. To isolate and further study the effect of sideways tilt, photos in this subset do not depict unusual pole shapes, excessively cluttered background, water reflection, and wavy water surface. Each selected photo contains a detected stop sign (by Mask R-CNN) and at least one detected line (by edge and line detectors), and is assigned to one of the two groups of qualified photos showing a stop sign without tilt, or those showing a stop sign with excessive sideways tilt (e.g.,  $\pm 25^\circ$ ).

### 5.1. Pole tilt correction

The general approach to tilt correction is to apply a reverse rotation to the image to visually rectify tilt. Given the standard shape of the stop sign, the amount of tilt (expressed in the 3D space by yaw, pitch, and roll angles, as in [Fig. 8](#)) is determined based on the appearance of the octagon sign. The positive direction of rotations about each axis is determined using the right-hand grip rule ([Cutnell & Johnson, 1998](#)). First, a template octagon of  $200 \times 200$  pixels is created in a binary color space and rotated along  $x$ ,  $y$ , and  $z$  axes. The range of rotations for pitch and yaw angles is set to  $(-45^\circ, +45^\circ)$  with  $2^\circ$  increments, because above this region the stop sign is hardly visible to Mask R-CNN. Since an octagon has rotational symmetry of order 8 with an internal angle of  $135^\circ$  and a central angle of  $45^\circ$ , the shape of the octagon repeats in every  $45^\circ$  of rotation along the  $z$  axis. By limiting the range of the central rotation angle (i.e., roll) to  $(-35^\circ, +35^\circ)$  with  $2^\circ$  increments, a total of 283,500 rotation combinations in the 3D space are created and used as benchmarks to approximate yaw, pitch, and roll angles of the detected stop sign mask. Next, the mask is resized to the template octagon and laps over each benchmark octagon. As shown in [Fig. 9](#), in each case, the pixel overlap (shown as  $Ol$ ) of the stop sign mask and the benchmark

**Table 3**

Performance of pole detection in pre- and post-flood photos before tilt correction.

Metric	Pre-flood (all, no-tilt, tilted)			Post-flood (all, no-tilt, tilted)		
	$n = 42$	$n = 38$	$n = 4$	$n = 42$	$n = 37$	$n = 5$
RMSE (in.)	21.67	20.38	33.90	15.30	15.08	16.93
Processing time (s)	1.78	1.76	1.93	2.07	1.94	2.19

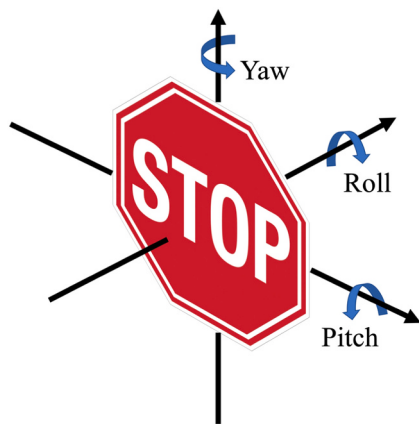


**Fig. 8.** Three different angles of rotation.

octagon is calculated. The comparison leading to the maximum overlap area (i.e.,  $Ol_{max}$ ) is selected as the one with closest rotation angles (in the 3D space) to the detected stop sign mask. Applying the reverse rotation to the image corrects the tilt problem by bringing the pole closer to vertical position. Since the size of the mask and the location of the bounding box may change as a result of this operation, the image is reprocessed by Mask R-CNN (Section 3.1) to detect the stop sign mask, and Canny edge detector and probabilistic Hough transform (Section 3.2) to estimate pole length.

Table 4 summarizes the performance of pole detection task in pre- and post-flood photos after tilt correction. Comparing Tables 3 and 4, it is evident that applying tilt correction reduces the error of pole detection in both pre- and post-flood photos. In particular, the overall error in pole detection after tilt correction is 17.43° (compared to 21.67° in Table 3) in pre-flood photos and 8.61° (compared to 15.30° in Table 3) in post-flood photos. It can thus be concluded that the designed tilt correction method improves the accuracy of pole detection, especially in post-flood photos where the presence of sideways tilt is more apparent.

## 5.2. Floodwater depth estimation

Knowing the pole length in paired pre- and post-flood photos taken

**Table 4**

Performance of pole detection in pre- and post-flood photos after tilt correction.

Metric	Pre-flood (all, no-tilt, tilted)			Post-flood (all, no-tilt, tilted)		
	n = 42	n = 38	n = 4	n = 42	n = 37	n = 5
RMSE (in.)	17.43	16.49	26.39	8.61	9.56	1.62
Processing time (s)	3.34	3.35	3.31	3.56	3.32	3.71

from the same location, the depth of floodwater  $d_w$  is calculated as the difference between the two pole lengths. Fig. 10 shows sample results from floodwater depth calculation. In Fig. 10(a), pole lengths in pre- and post-flood photos are estimated as 47.26 in. (compared to the ground truth of 47.81 in.) and 23.61 in. (compared to the ground truth of 24.88 in.), indicating 23.65 in. of floodwater.

Overall, floodwater depth estimation leads to a mean absolute error of 12.63 in.. In comparison, Cohen et al. (2019) reported an average absolute difference of 18–31 cm (approximately 7–12 in.) in estimating the depth of flood for coastal (using a 1-m DEM) and riverine (using a 10-m DEM) locations, Chaudhary et al. (2019) obtained a mean absolute error of 10 cm (approximately 4 in.) using social media images that depict submerged objects of various sizes, and Park et al. (2021) presented a mean absolute error value of 6.49 cm (approximately 2.5 in.) using images of flooded vehicles. However, it must be noted that the real value of the developed technique in this paper is its generalizability to new scenarios (stop signs are omnipresent and easy to locate), as well as its scalability by significantly increasing the number of points where floodwater depth can be calculated and mapped.

## 6. Summary and conclusion

In flood events, knowing the depth of floodwater is of critical importance to first responders, emergency managers, and ordinary people involved in SAR operations and community evacuation. This information, however, is not readily available or shared in many jurisdictions particularly in the immediate flood aftermath when it is most needed. Additionally, current flood mapping methods such as those relying on DEMs fail to capture reshaped surface topography and microtopographic variations in flat terrain especially in urban areas, leading to large vertical errors. New digital media capture and data exchange platforms coupled with advancements in ML, image

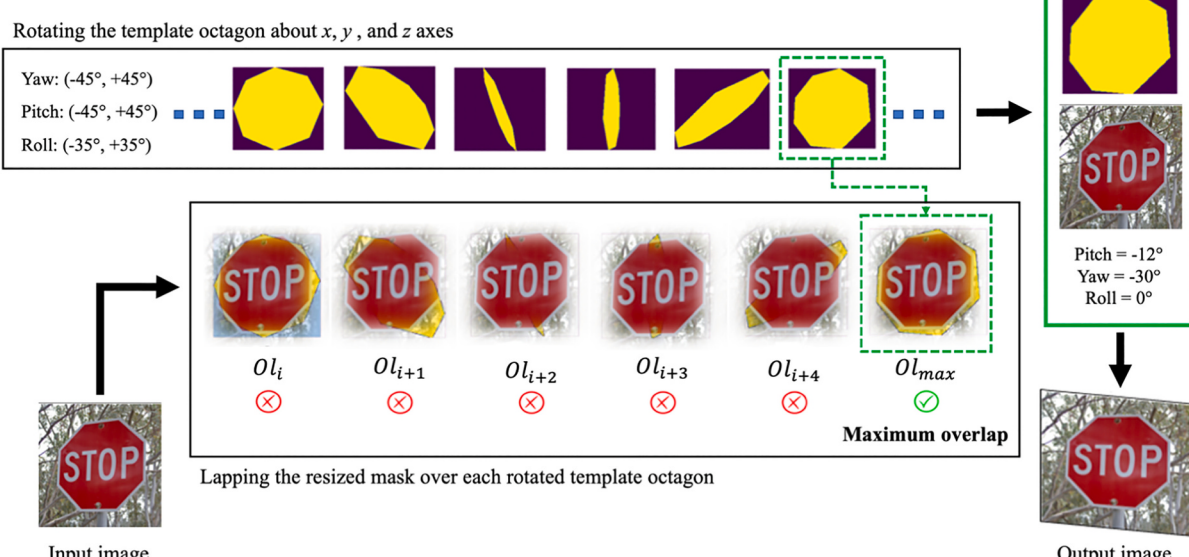


**Fig. 9.** Tilt angle estimation using template stop signs.

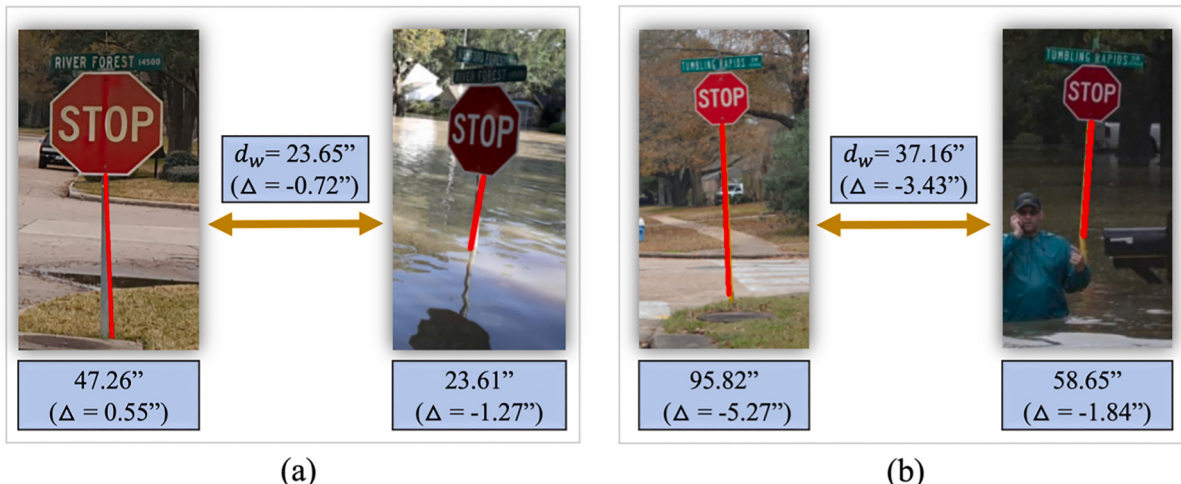


**Fig. 10.** Examples of floodwater depth estimation for paired pre- and post-flood photos. (base post-flood photos (a): courtesy of Win McNamee/Getty Images; (b): courtesy of Erich Schlegel/Getty Images).

processing, and computer vision for object detection have created new opportunities for remotely estimating water level depth in flooded areas.

In this paper, a new approach to estimating floodwater depth in street photos using stop signs as measurement benchmark was introduced and validated. An in-house dataset, named BluPix 2020.1, consisting of paired web-mined photos of submerged stop signs across 10 FEMA regions (for U.S. locations) and Canada was generated and used. To detect the octagon shape of the sign, a deep neural network called Mask R-CNN was utilized, and the image was subsequently processed by Canny edge detector and probabilistic Hough transform to detect vertical edges and discover potential pole candidates. Since stop signs have standard dimensions, the number of inches corresponding to one pixel in the photo was calculated and used to determine the pole length in inches, and the floodwater depth was ultimately estimated as the difference between pole length values of the same stop sign in a pair of pre- and post-flood photos taken from the same location. To limit the error in pole length detection, a tilt correction method was designed and applied to all photos to ensure poles are in near vertical position prior to the application of probabilistic Hough line transform. Overall, pole length was estimated with an RMSE of 17.43 and 8.61 in. in pre- and post-flood photos, respectively, leading to a mean absolute error of 12.63 in. in floodwater depth estimation.

Potential directions for future work in this research include addressing other causes of error in pole length estimation such as water reflection, pole shape, background effects, and image resolution. Additionally, more flood photos are being collected and paired using a crowdsourcing application developed by the authors, which will help improve the robustness and generalizability of the developed models. In order to implement the proposed approach in (near-) real time, an end-to-end computing platform will be designed to connect individual photo capturing devices (e.g., smartphones) to a cloud server that calculates and communicates floodwater depth information with the end users. In particular, the longitude, latitude, and gaze (i.e., direction of look) information of the photo capturing device can be used to automatically reconstruct the camera viewpoint in Google Street View or other online mapping systems and extract the corresponding pre-flood view. This is followed by running Mask R-CNN to detect stop signs in paired pre- and post-flood views, and calculating pole lengths and estimating the depth of floodwater, using the methodology laid out in this paper. Using a cloud server to collaboratively run object detection and image processing tasks is consistent with the literature (Guillermo et al., 2020; Lorenzik & Sincak, 2013; Singh, 2018), and expected to significantly reduce the computational burden on mobile devices, thus supporting the large-scale adoption of this research in disaster management

applications.

#### Declaration of Competing Interest

The authors declare that they have no known competing financial interests or personal relationships that could have appeared to influence the work reported in this paper.

#### Acknowledgments

This study is funded by award #NA18OAR4170088 from the National Oceanic and Atmospheric Administration (NOAA), U.S. Department of Commerce. The authors would also like to thank Mr. Nathan Young for his assistance in data collection. Any opinions, findings, conclusions, and recommendations expressed in this paper are those of the authors and do not necessarily represent the views of the NOAA, Department of Commerce, or the individual named above.

#### References

- AECOM. (2013). The impact of climate change and population growth on the National Flood Insurance Program through 2100. [https://aecom.com/content/wp-content/uploads/2016/06/Climate\\_Change\\_Report\\_AECOM\\_2013-06-11.pdf](https://aecom.com/content/wp-content/uploads/2016/06/Climate_Change_Report_AECOM_2013-06-11.pdf).
- Alfieri, L., Bisselink, B., Dottori, F., Naumann, G., de Roo, A., Salamon, P., ... Feyen, L. (2017). Global projections of river flood risk in a warmer world. *Earth's Future*, 5(2), 171–182. <https://doi.org/10.1002/2016EF000485>.
- American Climate. (2019). An inside climate news project. In *Deaths & major events* (Accessed: 14.06.2020) <https://insideclimatenews.org/american-climate/data/chart>.
- Barz, B., Schröter, K., Münch, M., Yang, B., Unger, A., Dransch, D., & Denzler, J. (2019). Enhancing flood impact analysis using interactive retrieval of social media images. *arXiv preprint*. <https://doi.org/10.5445/KSP/1000087327/06>. arXiv:1908.03361.
- Baugh, C. A., Bates, P. D., Schumann, G., & Trigg, M. A. (2013). SRTM vegetation removal and hydrodynamic modeling accuracy. *Water Resources Research*, 49(9), 5276–5289. <https://doi.org/10.1002/wrcr.20412>.
- Boeing, G. (2018). A multi-scale analysis of 27,000 urban street networks: Every US city, town, urbanized area, and Zillow neighborhood. *Environment and Planning B: Urban Analytics and City Science*, 47(4), 590–608.
- Chaudhary, P., D'Aronco, S., Moy de Vitry, M., Leitão, J. P., & Wegner, J. D. (2019). Flood-water level estimation from social media images. *ISPRS Annals of the Photogrammetry, Remote Sensing and Spatial Information Sciences*, 4(2/W5), 5–12. <https://doi.org/10.3929/ethz-b-000351581>.
- Chetpattananondh, K., Tapoanoi, T., Phukpattaranont, P., & Jindapetch, N. (2014). A self-calibration water level measurement using an interdigital capacitive sensor. *Sensors and Actuators A: Physical*, 209, 175–182. <https://doi.org/10.1016/j.sna.2014.01.040>.
- Church, J. A., & White, N. J. (2011). Sea-level rise from the late 19th to the early 21st century. *Surveys in Geophysics*, 32, 585–602. <https://doi.org/10.1007/s10712-011-9119-1>.
- Cleetus, R. (2013). Overwhelming risk: Rethinking flood insurance in a world of rising seas. In *Union of concerned scientists*. <https://www.ucsusa.org/resources/overwhelming-risk-rethinking-flood-insurance-world-rising-seas>.

- Cohen, S., Raney, A., Munasinghe, D., & Loftis, J. D. (2019). The floodwater depth estimation tool (fwdet v2. 0) for improved remote sensing analysis of coastal flooding. *Natural Hazards and Earth System Sciences*, 19(9), 2053. <https://doi.org/10.5194/nhess-19-2053-2019>.
- Collins, K. A., Hunt, W. F., & Hathaway, J. M. (2007). Evaluation of various types of permeable pavements with respect to water quality improvement and flood control. In *World environmental and water resources congress 2007: Restoring our natural habitat* (pp. 1–12). <https://doi.org/10.1061/40927%28243%29435>.
- Cortes, C., & Vapnik, V. (1995). Support-vector networks. *Machine Learning*, 20(3), 273–297. <https://doi.org/10.1007/BF00994018>.
- Cutnell, J., & Johnson, K. (1998). *Physics*, 2 (pp. 631–649). NY: Wiley.
- Delgado, D. F. M. (2018). *The promotion of instability of a highly-deformed plate under fluid loading and its transition to oscillatory motion*. Cornell University.
- Department of Homeland Security Office of Inspector General. (2017). *FEMA needs to improve management of its flood mapping programs* (p. 2017). Washington DC: DHS. <https://www.documentcloud.org/documents/4066233-OIG-17-110-Sep17.html>.
- Dong, S., Yu, T., Farahmand, H., & Mostafavi, A. (2020). Bayesian modeling of flood control networks for failure cascade characterization and vulnerability assessment. *Computer-Aided Civil and Infrastructure Engineering*, 35(7), 668–684. <https://doi.org/10.1111/mice.12527>.
- Dunham, M. H. (2007). *Data mining: Introductory and advanced topics* (1st ed. 2003). India: Pearson education India. ISBN-13: 978-0130888921.
- Everingham, M., Van Gool, L., Williams, C. K., Winn, J., & Zisserman, A. (2010). The pascal visual object classes (voc) challenge. *International Journal of Computer Vision*, 88(2), 303–338. <https://doi.org/10.1007/s11263-009-0275-4>.
- Fan, C., Esparza, M., Dargin, J., Wu, F., Oztekin, B., & Mostafavi, A. (2020). Spatial biases in crowdsourced data: Social media content attention concentrates on populous areas in disasters. *Computers, Environment and Urban Systems*, 83, 101514. <https://doi.org/10.1016/j.compenvurbsys.2020.101514>.
- Farras, A. W. (2020). Auto-thresholding canny edge detection. In *MATLAB central file exchange* (Accessed: 09.07.2020) <https://www.mathworks.com/matlabcentral/fileexchange/61237-auto-thresholding-canny-edge-detection>.
- Federal Emergency Management Agency. (2010). Are you ready guide (Accessed: 01.08.2020) [https://www.fema.gov/pdf/areyouready/areyouready\\_full.pdf](https://www.fema.gov/pdf/areyouready/areyouready_full.pdf).
- Federal Emergency Management Agency. (2016). Pre-disaster recovery planning guide for state governments. [https://www.fema.gov/sites/default/files/2020-06/pre-disaster\\_recovery\\_planning\\_guide\\_state\\_governments.pdf](https://www.fema.gov/sites/default/files/2020-06/pre-disaster_recovery_planning_guide_state_governments.pdf).
- Federal Highway Administration. (2004). Manual on Uniform Traffic Control Devices ( MUTCD): Standard highway signs (Accessed: 01.08.2020) [https://mutcd.fhwa.dot.gov/ser-shm/millennium\\_eng.htm](https://mutcd.fhwa.dot.gov/ser-shm/millennium_eng.htm).
- Federal Highway Administration. (2009). *Stop Signs, Issue Briefs 4*. Washington, DC: U.S Department of Transportation, FHWA-SA-10-005. [https://safety.fhwa.dot.gov/intersection/other\\_topics/fhwasa10005/docs/brief\\_4.pdf](https://safety.fhwa.dot.gov/intersection/other_topics/fhwasa10005/docs/brief_4.pdf).
- First Street Foundation. (2019). Fema flood maps and limitations (Accessed: 01.08.2020) <https://medium.com/firststreet/fema-flood-maps-and-limitations-ea06bf103c4d>.
- FloodZone. (2018). *Why you should purchase flood insurance*. <https://floodzoneds.com/why-you-should-purchase-flood-insurance/>. Access date: March 25, 2021.
- Ford, A., Barr, S., Dawson, R., Virgo, J., Batty, M., & Hall, J. (2019). A multi-scale urban integrated assessment framework for climate change studies: A flooding application. *Computers, Environment and Urban Systems*, 75, 229–243. <https://doi.org/10.1016/j.compenvurbsys.2019.02.005>.
- Galloway, G. E., Reilly, A., Ryoo, S., Brody, S., Highfield, W., Gunn, J., ... Parker, S. (2018). *The growing threat of urban flooding: A national challenge*. College Park and Galveston: University of Maryland and Texas A&M University.
- Garner, A. J., Kopp, R. E., Horton, B. P., Mann, M. E., Alley, R. B., Emanuel, K. A., ... Pollard, D. (2018). New York City's evolving flood risk from hurricanes and sea level rise. *Sea Level Rise*, 16(1), 30–35. <https://doi.org/10.5065/D6445K8Z>.
- Gebehiwot, A., Hashemi-Beni, L., Thompson, G., Kordjamshidi, P., & Langan, T. E. (2019). Deep convolutional neural network for flood extent mapping using unmanned aerial vehicles data. *Sensors*, 19(7), 1486. <https://doi.org/10.3390/s19071486>.
- Girshick, R. (2015). *Fast r-cnnR-CNN*. In *proceedings of the IEEE international conference on computer vision* (pp. 1440–1448). <https://arxiv.org/abs/1504.08083>.
- Guillermo, M., Billones, R. K., Bandala, A., Vicerra, R. R., Sybingco, E., Dadios, E. P., & Fillone, A. (2020). Implementation of automated annotation through mask RCNN object detection model in CVAT using AWS EC2 instance. In *2020 IEEE region 10 conference (TENCON)* (pp. 708–713). <https://doi.org/10.1109/TENCON50793.2020.9293906>.
- Gulli, A., & Pal, S. (2017). *Deep learning with Keras*. Packt Publishing Ltd.. ISBN 978-1-78712-842-2.
- Hauer, M. E., Evans, J. M., & Mishra, D. R. (2016). Millions projected to be at risk from sea-level rise in the continental United States. *Nature Climate Change*, 6(7), 691–695. <https://doi.org/10.1038/nclimate2961>.
- Hawker, L., Bates, P., Neal, J., & Rougier, J. (2018). Perspectives on digital elevation model (DEM) simulation for flood modeling in the absence of a high-accuracy open access global DEM. *Frontiers in Earth Science*, 6, 233.
- He, K., Gkioxari, G., Dollár, P., & Girshick, R. (2017). *Mask r-cnnR-CNN*. In *proceedings of the IEEE international conference on computer vision* (pp. 2961–2969). [https://openaccess.thecvf.com/content\\_iccv\\_2017/html/He\\_Mask\\_R-CNN\\_ICCV\\_2017\\_paper.html](https://openaccess.thecvf.com/content_iccv_2017/html/He_Mask_R-CNN_ICCV_2017_paper.html).
- Hsiao, P. Y., Chen, C. H., Chou, S. S., Li, L. T., & Chen, S. J. (2006). A parameterizable digital-approximated 2D Gaussian smoothing filter for edge detection in noisy image. In *2006 IEEE international symposium on circuits and systems*. IEEE. <https://doi.org/10.1109/ISCAS.2006.1693303.57>, 4-pp.
- Huang, Z., Huang, L., Gong, Y., Huang, C., & Wang, X. (2019). Mask scoring scoring r-cnnR-CNN. In *Proceedings of the IEEE conference on computer vision and pattern recognition* (pp. 6409–6418).
- Hudson, P., Botzen, W. W., & Aerts, J. C. (2019). Flood insurance arrangements in the European Union for future flood risk under climate and socioeconomic change. *Global Environmental Change*, 58, 101966. <https://doi.org/10.1016/j.gloenvcha.2019.101966>.
- Incetas, M. O., Demirci, R., & Yavuzcan, H. G. (2019). Automatic color edge detection with similarity transformation. *Gazi University Journal of Science*, 32(2). <https://dergipark.org.tr/tr/download/article-file/726178>.
- Kenward, T., Lettenmaier, D. P., Wood, E. F., & Fielding, E. (2000). Effects of digital elevation model accuracy on hydrologic predictions. *Remote Sensing of Environment*, 74(3), 432–444. [https://doi.org/10.1016/S0034-4257\(00\)00136-X](https://doi.org/10.1016/S0034-4257(00)00136-X).
- Kwan, M. P., & Ransberger, D. M. (2010). LiDAR assisted emergency response: Detection of transport network obstructions caused by major disasters. *Computers, Environment and Urban Systems*, 34(3), 179–188. <https://doi.org/10.1016/j.compenvurbsys.2010.02.001>.
- Li, X., Yin, P., Zhi, Y., & Duan, C. (2020). Vertical lane line detection technology based on Hough transform. *IOP Conference Series: Earth and Environment Science*, 440(3), 032126. <https://doi.org/10.1088/1755-1315/440/3/032126>.
- Liang, J. (n. d.). Canny edge detection. (Accessed: 09.07.2020). <http://justin-liang.com/tutorials/canny/#double-thresholding>.
- Lin, T. Y., Goyal, P., Girshick, R., He, K., & Dollár, P. (2017). Focal loss for dense object detection. In *Proceedings of the IEEE international conference on computer vision* (pp. 2980–2988).
- Lin, T. Y., Maire, M., Belongie, S., Hays, J., Perona, P., Ramanan, D., ... Zitnick, C. L. (2014). Microsoft coco: Common objects in context. In *European conference on computer vision* (pp. 740–755). Cham: Springer. [https://doi.org/10.1007/978-3-319-10602-1\\_48](https://doi.org/10.1007/978-3-319-10602-1_48).
- Long, J., Shelhamer, E., & Darrell, T. (2015). Fully convolutional networks for semantic segmentation. In *Proceedings of the IEEE conference on computer vision and pattern recognition* (pp. 3431–3440). [https://openaccess.thecvf.com/content\\_cvpr\\_2015/papers/Long\\_Fully\\_Convolutional\\_Networks\\_2015\\_CVPR\\_paper.pdf](https://openaccess.thecvf.com/content_cvpr_2015/papers/Long_Fully_Convolutional_Networks_2015_CVPR_paper.pdf).
- Lorenzik, D., & Sincak, P. (2013). Cloud robotics: Current trends and possible use as a service. In *2013 IEEE 11th International Symposium on Applied Machine Intelligence and Informatics (SAMI)* (pp. 85–88). IEEE. <https://doi.org/10.1109/SAMI.2013.6480950>.
- McDougall, K., & Temple-Watts, P. (2012). The use of LIDAR and volunteered geographic information to map flood extents and inundation. *ISPRS Annals of the Photogrammetry, Remote Sensing and Spatial Information Sciences*, 1, 251–256.
- Meesuk, V., Vojinovic, Z., & Mynett, A. E. (2017). Extracting inundation patterns from flood watermarks with remote sensing SfM technique to enhance urban flood simulation: The case of Ayutthaya, Thailand. *Computers, Environment and Urban Systems*, 64, 239–253. <https://doi.org/10.1016/j.compenvurbsys.2017.03.004>.
- Mizutori, M., & Guha-Sapir, D. (2018). Economic losses, poverty and disasters 1998–2017, Centre for Research on epidemiology of disasters CRED, United Nations Office for Disaster Risk Reduction. [https://www.unisdr.org/files/61119\\_creedeconomicslosses.pdf](https://www.unisdr.org/files/61119_creedeconomicslosses.pdf).
- National Oceanic and Atmospheric Administration. (2020). National oceanic and atmospheric administration's national weather service (Accessed: 01.08.2020) <https://water.weather.gov/ahps/index.php>.
- Nayak, S., & Zlatanova, S. (Eds.). (2008). *Remote sensing and GIS technologies for monitoring and prediction of disasters*. Springer Science & Business Media. <https://link.springer.com/content/pdf/10.1007/978-3-540-79259-8.pdf>.
- Odli, Z. S. M., Izhar, T. N. T., Razak, A. R. A., Yusuf, S. Y., Zakarya, I. A., Saad, F. N. M., & Nor, M. Z. M. (2016). Development of portable water level sensor for flood management system. *ARPJN Journal of Engineering and Applied Sciences*, 11(8), 5352–5357. [http://www.arpnjournals.org/jeas/research\\_papers/rp\\_2016/jeas\\_0416\\_4118.pdf](http://www.arpnjournals.org/jeas/research_papers/rp_2016/jeas_0416_4118.pdf).
- Ogawa, K., Ito, Y., & Nakano, K. (2010). Efficient canny edge detection using a GPU. In *2010 first international conference on networking and computing* (pp. 279–280). IEEE. <https://doi.org/10.1109/IC-NC.2010.13>.
- O'Loughlin, F. E., Paiva, R. C. D., Durand, M., Alsdorf, D. E., & Bates, P. D. (2016). A multi-sensor approach towards a global vegetation corrected SRTM DEM product. *Remote Sensing of Environment*, 182, 49–59. <https://doi.org/10.1016/j.rse.2016.04.018>.
- OpenCV Dev Team. (2019). Canny edge detector (Accessed: 02.08.2020) [https://docs.opencv.org/2.4/doc/tutorials/imgproc/imgtrans/canny\\_detector/canny\\_detector.html](https://docs.opencv.org/2.4/doc/tutorials/imgproc/imgtrans/canny_detector/canny_detector.html).
- Pan, J., Yin, Y., Xiong, J., Luo, W., Gui, G., & Sari, H. (2018). Deep learning-based unmanned surveillance systems for observing water levels. *IEEE Access*, 6, 73561–73571. <https://doi.org/10.1109/ACCESS.2018.2883702>.
- Park, S., Baek, F., Sohn, J., & Kim, H. (2021). Computer vision-based estimation of flood depth in flooded-vehicle images. *Journal of Computing in Civil Engineering*, 35(2), Article 04020072. [https://doi.org/10.1061/\(ASCE\)CP.1943-5487.0000956](https://doi.org/10.1061/(ASCE)CP.1943-5487.0000956).
- Pedersini, F., Sarti, A., & Tubaro, S. (1997). Estimation and compensation of subpixel edge localization error. *IEEE Transactions on Pattern Analysis and Machine Intelligence*, 19(11), 1278–1284. <https://doi.org/10.1109/34.632986>.
- Pi, Y., Nath, N. D., & Behzadan, A. H. (2020). Convolutional neural networks for object detection in aerial imagery for disaster response and recovery. *Advanced Engineering Informatics*, 43, 101009. <https://doi.org/10.1016/j.aei.2019.101009>.
- Powers, D. M. (2011). Evaluation: from precision, recall and F-measure to ROC, informedness, markedness and correlation. <https://dspace.flinders.edu.au/xmlui/handle/2328/27165>.
- Public Safety Canada (2010). Emergency management planning guide 2010–2011. (Accessed: 14.06.2020). (Canada). <https://www.publicsafety.gc.ca/cnt/rsrcs/plcbs/mrgnc-mngmnt-pnng/mrgnc-mngmnt-pnng-eng.pdf>.

- Puttinaovarat, S., & Horkaew, P. (2020). Flood forecasting system based on integrated big and crowdsource data by using machine learning techniques. *IEEE Access*, 8, 5885–5905. <https://doi.org/10.1109/ACCESS.2019.2963819>.
- Ren, S., He, K., Girshick, R., & Sun, J. (2015). Faster r-cnnR-CNN: Towards real-time object detection with region proposal networks. In *Advances in neural information processing systems* (pp. 91–99). [http://refhub.elsevier.com/S1474-0346\(19\)30582-8/h0115](http://refhub.elsevier.com/S1474-0346(19)30582-8/h0115).
- Rong, W., Li, Z., Zhang, W., & Sun, L. (2014). An improved canny edge detection algorithm. In *2014 IEEE international conference on mechatronics and automation* (pp. 577–582). IEEE. <https://doi.org/10.1109/ICMA.2014.6885761>.
- Salmonsson, A. (2015). Mike 21 fm in urban flood risk analysis: a comparative study relating to the MIKE 21 Classic model (Accessed: 14.06.2020) <http://kth.diva-portal.org/smash/get/diva2:839685/FULLTEXT01.pdf>.
- Sazara, C., Cetin, M., & Iftekharuddin, K. M. (2019). Detecting floodwater on roadways from image data with handcrafted features and deep transfer learning. In *2019 IEEE Intelligent Transportation Systems Conference (ITSC)* (pp. 804–809). IEEE. <https://doi.org/10.1109/ITSC.2019.8917368>.
- Schumann, G. J. P. (2014). Fight floods on a global scale. *Nature*, 507, 169. <https://doi.org/10.1038/507169e>.
- Shinar, D., Dewar, R. E., Summala, H., & Zakowska, L. (2003). Traffic sign symbol comprehension: A cross-cultural study. *Ergonomics*, 46(15), 1549–1565. <https://doi.org/10.1080/0014013032000121615>.
- Simonyan, K., & Zisserman, A. (2015). Very deep convolutional networks for large-scale image recognition. arxiv Preprint. *ICLR2015 conference (International Conference on Learning Representations) in San Diego, CA* <http://arxiv.org/abs/1409.1556>.
- Singh, K. K. (2018). An artificial intelligence and cloud based collaborative platform for plant disease identification, tracking and forecasting for farmers. In *2018 IEEE international conference on cloud computing in emerging markets (CCEM)* (pp. 49–56). <https://doi.org/10.1109/CCEM.2018.00016>.
- Smith, A. B. (2020). 2010-2019: A landmark decade of US billion-dollar weather and climate disasters. In *National oceanic and atmospheric administration* Accessed: 14.06.2020 <https://www.climate.gov/news-features/blogs/beyond-data/2010-20-19-landmark-decade-us-billion-dollar-weather-and-climate>.
- Sobel, I. (1978). Neighborhood coding of binary images for fast contour following and general binary array processing. *Computer Graphics and Image Processing*, 8(1), 127–135. [https://doi.org/10.1016/S0146-664X\(78\)80020-3](https://doi.org/10.1016/S0146-664X(78)80020-3).
- Tanyeri, U., Kılıçaslan, M., & Demirci, R. (2019). Canny edge detector with half entropy. In *2019 3rd international symposium on multidisciplinary studies and innovative technologies (ISMSIT)* (pp. 1–4). IEEE. <https://ieeexplore.ieee.org/stamp/stamp.jsp?arnumber=8932770>.
- Ten Veen, P. M., Morren, M., & Yzermans, C. J. (2009). The influence of news events on health after disaster: A longitudinal study in general practice. *Journal of Traumatic Stress: Official Publication of The International Society for Traumatic Stress Studies*, 22(6), 505–515. <https://doi.org/10.1002/jts.20462>.
- Texas General Land Office. (2019). State of Texas CDBG mitigation (CDBG-MIT) action plan: Building stronger for a resilient future. [https://recovery.texas.gov/public-notices/files/cdbg-mit\\_ap\\_pc\\_draft\\_english.pdf](https://recovery.texas.gov/public-notices/files/cdbg-mit_ap_pc_draft_english.pdf).
- Töyrä, J., Pietroniro, A., Martz, L. W., & Prowse, T. D. (2002). A multi-sensor approach to wetland flood monitoring. *Hydrological Processes*, 16(8), 1569–1581. <https://doi.org/10.1002/hyp.1021>.
- United States Geological Survey. (2019). *Introducing the next generation of USGS water data for the nation* Accessed: 15.05.2020 <https://help.waterdata.usgs.gov/news/Fe-b-12-2019>.
- Vincent, O. R., & Folorunso, O. (2009). A descriptive algorithm for sobel image edge detection. In , vol. 40. *Proceedings of Informing Science & IT Education Conference (InSITE)* (pp. 97–107). California: Informing Science Institute (June 2009) <https://proceedings.informingscience.org/InSITE2009/InSITE09p097-107Vincent613.pdf>.
- Walker, J. P., & Willgoose, G. R. (1999). On the effect of digital elevation model accuracy on hydrology and geomorphology. *Water Resources Research*, 35(7), 2259–2268. <https://doi.org/10.1029/1999WR900034>.
- Wang, R. (2013). Canny edge detection (Accessed: 02.08.2020) <http://fourier.eng.hmc.edu/e161/lectures/canny/node1.html>.
- Yang, H. C., Wang, C. Y., & Yang, J. X. (2014). Applying image recording and identification for measuring water stages to prevent flood hazards. *Natural Hazards*, 74(2), 737–754. <https://doi.org/10.1007/s11069-014-1208-2>.
- Zhu, Z., & Brilakis, I. (2009). Automated detection of concrete columns from visual data. *Journal of Computing in Civil Engineering*, 135–145. [https://doi.org/10.1061/41052\(346\)14](https://doi.org/10.1061/41052(346)14).